ISSN 1392-1207. MECHANIKA. Vol. 30, No. 6, 2024: 498–506

Effect of Manta Ray's Flexible Hydrofoil Kinematic Parameters on Autonomous Propulsion Efficiency

Hao DING*, Qiang GAO, Haipeng SHI***, Huipeng SHEN****, Ruoqian CHEN*****

**School of Mechanical and Electrical Engineering, Henan University of Technology, Zhengzhou 450001, P. R. China, E-mail: dinghao@haut.edu.cn*

*** School of Mechanical and Electrical Engineering, Henan University of Technology, Zhengzhou 450001, P. R. China, E-mail: 1411472561@qq.com (Corresponding author)*

****School of Mechanical and Electrical Engineering, Henan University of Technology, Zhengzhou 450001, P. R. China, E-mail: 1729426759@qq.com*

*****School of Mechanical and Electrical Engineering, Henan University of Technology, Zhengzhou 450001, P. R. China, E-mail: hpengshen@haut.edu.cn*

******School of Mechanical and Electrical Engineering, Henan University of Technology, Zhengzhou 450001, P. R. China, E-mail: 15378775937@163.com*

https://doi.org/10.5755/j02.mech.37715

1. Introduction

With the continuous advancement of human demands for tasks such as ocean resource exploitation, underwater resource exploration, and marine ecological monitoring, various types of Unmanned Underwater Vehicles (UUVs) have emerged. Conventional underwater vehicles employ propeller propulsion however, this propulsion method generates a significant amount of cavitation bubbles during operation, leading to propeller cavitation erosion and reduced propulsion system longevity [1, 2]. Additionally, propeller noise can impact aquatic life and cause harm to marine organisms during navigation [3-6]. In contrast, underwater vehicles utilizing biomimetic propulsion as their power system can avoid the aforementioned shortcomings. Flexible propulsion methods offer advantages such as high efficiency, low noise, and excellent maneuverability. This is of paramount significance for the design and development of ocean exploration and monitoring devices [7-10].

Regarding the swimming motion of marine organisms, their thrust generation methods can be categorized into two types. One is the added mass effect method, where fish generate backward water movement around their bodies through undulating motions, thereby obtaining forward propulsion [11, 12]. The other method is based on Leading-Edge Vortex (LEV) thrust generation. When the caudal fin of fish moves laterally, it generates a leading-edge vortex that strengthens with increased interaction with the central fin [13]. Mantas, a collective term for several genera of cartilaginous fishes in the order Rajiformes, exhibit distinctive swimming motions compared to typical fish tail fin propulsion methods [14-16]. With a flattened body profile, mantas rely on the oscillation of their large pectoral fins to generate propulsion force [17]. Rosenberger introduced the continuous theory and categorized the oscillatory motion of mantas [18]. Different species of mantas adjust various motion variables to modulate their swimming velocities. Zhang et al. [19] studied the vortex shedding and hydrodynamic performance of mantas. At lower Strouhal numbers, slight flexible hydrofoil deformation results in increased effective angle of attack, intensifying vortex strength. This, in turn, enhances the thrust generated through LEV Russo et al. [20] investigated the swimming of fish such as mantas and rays using their pectoral fins and employed biomechanical models to simulate the swimming motion of manta skeletons, estimating uniaxial strain effects. These studies primarily explore the hydrodynamic principles of manta swimming.

In the realm of bionic manta-inspired underwater vehicles, Pan et al. [7, 21-24] designed an integrated gliding-flapping manta robot. This robotic system possesses enhanced efficiency for remote gliding, leading to improved energy conservation and endurance in underwater operational tasks when compared to conventional underwater robots. Thekkethil et al. [25] conducted a study on the flow field during manta hydrofoil flapping, offering valuable insights for the design of biomimetic Autonomous Underwater Vehicles (AUVs). Fish. et al. [26, 27] proposed the inspiration of manta fish for the design of the next generation of underwater vehicles. They compiled practical data on manta movements to provide reference points for AUV design and also conducted direct observations of manta swimming. Research has indicated that mobuliform swimming could offer valuable insights for the creation of highly efficient and operationally superior underwater vehicles. The maximum efficiency achieved by mobuliform swimming is around 89%, surpassing the efficiency of rajiform swimming [28, 29]. Hydrodynamic literature related to manta swimming indicates that the undulatory swimming style of mantas is less forceful compared to the body and tail oscillations of other fish. Manta pectoral fin oscillations exhibit considerable differences in wavelength and frequency when compared to the tail oscillations of other fish. Mantas tend to favor low-frequency and long-wavelength oscillations, while tail-fin propulsion fish lean towards high-frequency and short-wavelength oscillations. Moreover, the efficiency of manta swimming exceeds that of rajiform swimming.

Summing up the aforementioned analysis, researchers have conducted numerous studies on the hydrodynamic performance and prototype fabrication of manta swimming. However, there remains a lack of detailed and in-depth investigation into the relationship between the kinematic parameters of manta swimming and its autonomous swimming efficiency. Different motion parameters can lead to distinct flapping propulsion actions in mantas, which in turn can influence the propulsion efficiency of their swimming. Building on this premise, in this study, Computational

Fluid Dynamics (CFD) methodology is proposed to explore the correlation between the chordwise motion parameters of manta pectoral fins and the efficiency of autonomous manta swimming. This investigation aims to provide guidance for the design of flapping actions in underwater vehicles, drawing inspiration from manta swimming dynamics.

The remainder of the paper is organized as follows. The physical model and numerical simulation method for manta rays is presented in Section 2. The effectiveness of the numerical simulation method is then verified as detailed in Section 3. The effect of the wavelength and frequency of the propulsive motion of the flexible hydrofoil on the vortex volume, autonomous propulsive speed and autonomous propulsion efficiency of the flexible hydrofoil is discussed in Section 4. Finally, the conclusions drawn from our study are provided in Section 5.

2. Numerical Model

2.1. Physical model

Fig. 1, a illustrates a top view of the manta ray fish. Based on its external structure, a three-dimensional model of the manta ray has been established, as depicted in Fig. 1, b. The hydrofoil span measures 3.5 meter. The total body length, including the tail, is 4.0 meters. The body shape of the manta ray is diamond-shaped, and it has two head fins derived from the differentiation of pectoral fins. The pectoral fins are triangular and resemble hydrofoil-like structures. To simplify the model, this research employs a two-dimensional cross-section of the pectoral fin, as shown in Fig. 1, c. The cross-section exhibits a hydrofoil shape with a streamlined contour.

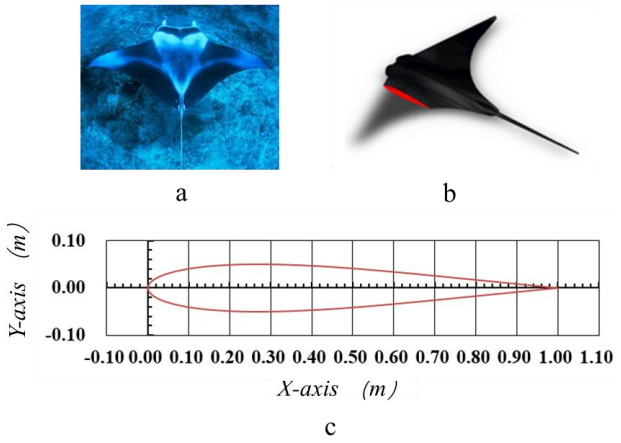

Fig. 1 Manta ray solid diagram and physical calculation model: a – physical view of manta rays, b – manta ray physical computational model, c – manta ray pectoral fin profile

2.2. *k-ω* turbulent model

The calculation uses the *k-ω* turbulent model [30], which employs two equations to describe turbulent flow. The first equation is the *k* equation used to compute the transport and generation of turbulent kinetic energy. The second equation is the *ω* equation used to compute the transport and generation of turbulent dissipation rate. These two equations correct some deficiencies in the traditional *k-ε* model by considering the radial gradient transport of turbulence.

The basic equations of the *k-ω* model are as follows:

$$\frac{\partial k}{\partial t} + u \cdot \nabla k = P - \beta\omega k + \nabla \cdot \left(\nu + \frac{\sigma_k}{\omega} \right) \cdot \nabla k \,, \tag{1}$$

$$\frac{\partial \omega}{\partial t} + u \cdot \nabla \omega = \gamma - \alpha\omega^2 - \beta\omega k + \nabla \cdot \left(\nu + \frac{\sigma_\omega}{\omega} \right) \cdot \nabla \omega \,. \tag{2}$$

Among them, *k* represents turbulent kinetic energy, *ω* represents turbulent dissipation rate, *u* represents flow velocity, *v* represents dynamic viscosity coefficient, and σ_k and σ_ω are D_{ij} matrices proportional to *k* and *ω* respectively.

2.3. Mathematical equations of motion

The flexible hydrofoil wave equation is defined as follows:

$$h(x,t) = A(x) \cdot sin(kx - \omega t) \,, \tag{3}$$

$$A(x) = a_1 x + a_2 x^2 + a_3 x^3 \cdots \,, \tag{4}$$

$$k = \frac{2\pi}{\lambda} \,,\ \omega = \frac{2\pi}{T} \,,\ T = \frac{1}{f} \,, \tag{5}$$

where *A*(*x*) represents the amplitude of the wave, a is a coefficient (constant), where $a_1 = 0.044$, $a_2 = 0.058$, and $a_3 = 0.064$, *k* is the wave number corresponding to the wavelength *λ* of the undulating object, *ω* is the angular frequency, *T* is the period, and the length of the flexible hydrofoil is defined as *L*. The wavelength *λ* is expressed as a multiple of *L*.

During the simulation process of self-propelled swimming with a flexible hydrofoil, the mass of the flexible hydrofoil is calculated based on Newton's second law, and the acceleration is determined by solving for the thrust. The velocity increment is defined as the product of the average acceleration and the time increment, and the velocity is the sum of all velocity increments. The displacement increment is the product of the average velocity at the current time step and the time step length, and the position is the sum of all displacement increments. The expressions are as follows:

$$F_X = F_T - F_D \,, \tag{6}$$

$$a = \frac{F_X}{m} \,, \tag{7}$$

$$m = \bar{\rho} \mathrm{V} \,, \tag{8}$$

$$v(t) = v_t + \frac{a_t + a_{t+\Delta t}}{2} \times \Delta t \,, \tag{9}$$

$$dS(t) = \frac{v_t + v_{t+\Delta t}}{2} \times \Delta t \,, \tag{10}$$

$$S = S_t + dS \,. \tag{11}$$

F_X is the resultant force along the horizontal direction， F_T is the average thrust, F_D is the resistance, a is the acceleration, m is the mass, V is the volume, $\bar{\rho}$ is the average density, Δt is the time-varying increment, dS is the displacement increment, S is the total displacement.

When we use a two-dimensional profile model to calculate the question, the calculation model is shown in Fig. 2, a. The default airfoil length is 1 m and the cross-sectional area is 0.0645. Because the flexible fin can float and dive freely in the water, the average density of bone and flesh was determined to be 1000 kg/m^3.

The undulatory propulsion efficiency of the flexible fin uses the Froude efficiency [31]. For the flexible fin, the calculation is performed on each unit comprising its body. The force decomposition is shown in Fig. 2, b, the swimming efficiency is calculated by the sum of the velocities and forces of each unit of the body.

$$\eta = \frac{P_T}{P_T + P_S}, \tag{12}$$

$$P_T = \sum_i F_{Ti} v_{xi}, \tag{13}$$

$$P_s = \sum_i F_{si} v_{yi}, \tag{14}$$

η is the efficiency, P_T is the transverse swimming power, P_S is the longitudinal hydrofoil power, F_{Ti} and V_{xi} is the transverse force of the element and transverse velocity, F_{si} and v_{yi} is the longitudinal force and longitudinal velocity.

2.4. Boundary conditions and numerical schemes

The flexible fin has a large deformation range in the process of fluctuating propulsion. To avoid generating negative volume grid and improve the accuracy of calculation, the overlapping grid technique is employed in numerical calculations, as illustrated in Fig. 2, e – f. The mesh component in ANSYS is used to divide the grid, this approach introduces overlapping regions among neighboring grids, facilitating the interconnection of grids across distinct areas. This interconnection enhances the accuracy and precision of the numerical calculations passively. It is suitable for the calculation of flow fields with complex geometry or complex physical characteristics. After the meshing is completed, it is imported into the Fluent solver for solution.

In this simulation, the wave motion of the flexible hydrofoil is defined through a User-Defined Function (UDF). During the oscillation process of a flexible hydrofoil, the water flow is pushed backward by the hydrofoil to generate vortices. At the same time, the hydrofoil experiences a reactive force from the water flow to propel it forward. This interaction enables self-propelled swimming. The left side of the flow field is the inlet. Since the flexible hydrofoil autonomously swims, there is no need to specify an inflow velocity. The upper and lower boundaries of the flow domain are walls, representing fixed wall surfaces. The right side of the flow field is the outlet. The boundary condition for the outlet is set to a pressure outlet of 0 Pa. The flow domain is divided into a Background Grid, while the area near the flexible hydrofoil is divided into a Component Grid. Overlapping regions are defined as Overset interfaces, enabling the proper interaction between the grids. The

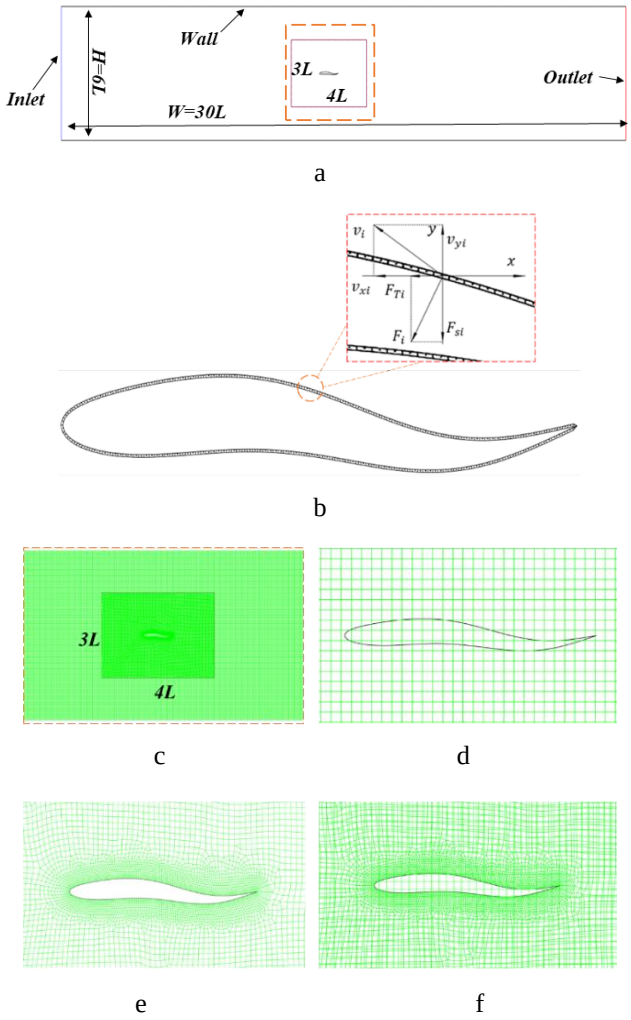

Fig. 2 Numerical calculation model of flexible fins and their meshing: a – flow field model, b – efficiency calculation method, c – overlapping grids, d – background grid, e – component grid, f – over-lapping grid region

solution methodology employs the Coupled method, which accurately describes the interaction between fluid and solid components.

3. Model Validation

To validate the effectiveness of the model, this study will compare the numerical simulation model with Egan's [32] experimental test results. The incoming flow velocity was set at 0.32 m/s, with an oscillation frequency of 1 Hz. Using the prescribed values of the angle of attack and stiffness constant from Egan's study, a wave motion curve closely resembling the deformation of the flexible hydrofoil was established. A NACA0015 airfoil with dimensions of 0.178 m (chord length) × 0.4 m (hydrofoil span) was used for the numerical calculations, as shown in Fig. 3, a. The numerical simulation results are depicted in Fig. 3, b - c and e It was found that the numerical results closely match Egan's experimental data, particularly in terms of the trajectory of the trailing vortex. The thrust trajectory has a small deviation near plus or minus 15°, and the rest of the trajectory is essentially the same. The lift trajectory has a small deviation near plus or minus 12°, and the rest of the trajectory is basically the same. These deviations are due to the

vibration of the experimental process and the sampling delay of the sensor, which are reasonable errors. In summary, the CFD model used in this study has been verified and is reasonable.

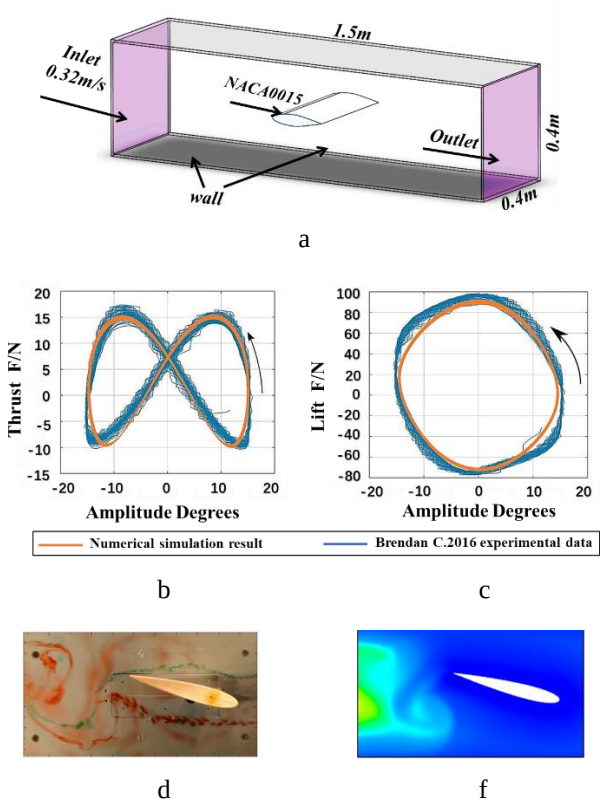

Fig. 3 Validation of computational models versus experimental results: a – validation of computational models, b – comparison of thrust values, c – comparison of lift values, d – experimental vortex trailing by Egan [32], e – numerical simulation of vortex trails

4. Results and Discussion

Building upon the validation of computational methods and preliminary investigation into the propulsion by flapping flexible fins and considering the up and down fluctuations in the two-dimensional section caused by the global swimming of the manta ray, we further analyze the influence of wavelength and frequency on the self-propulsion of such fins. In this study, the frequency range of the flexible fin's oscillation is set between 1 Hz and 4 Hz, while the wavelength varies from 1.0L to 1.8L, which is more in line with the motion parameter characteristics of manta rays.

4.1. Wake vortex structure analysis

The vorticity contour cloud map of the flexible hydrofoil during its transition from rest to steady swimming is shown in Fig. 4. The length of the flow field is 30L. From the vorticity contour map of the flexible hydrofoil, it can be observed that the flexible hydrofoil induces a counter-rotating Kármán vortex street during its autonomous swimming process. Vortices are generated at the front of the flexible hydrofoil, becoming attached to the surface, flowing rearward, and ultimately detaching from the tail of the fin due to the hydrofoil's flapping motion. The rotation direction of the detached vortices depends on the direction of the hydrofoil's motion at the tail, and the velocity of the detached vortices depends on the flapping speed of the flexible hydrofoil.

Additionally, it can be found that when the flexible hydrofoil's trailing vortices detach, turbulence is generated on both sides. This turbulence is caused by the rapid movement of fluid due to the fast tail motion of the flexible hydrofoil. Over time, the longitudinal turbulence is gradually entrained into the trailing vortices, causing the size of the trailing vortices to increase. Consequently, the longitudinal turbulence near the earlier formed trailing vortices becomes smaller, while the turbulence near the newly formed ones becomes larger, resulting in smaller vortices. As this process involves kinetic energy losses, the vorticity values of the trailing vortices formed earlier are smaller compared to those formed more recently.

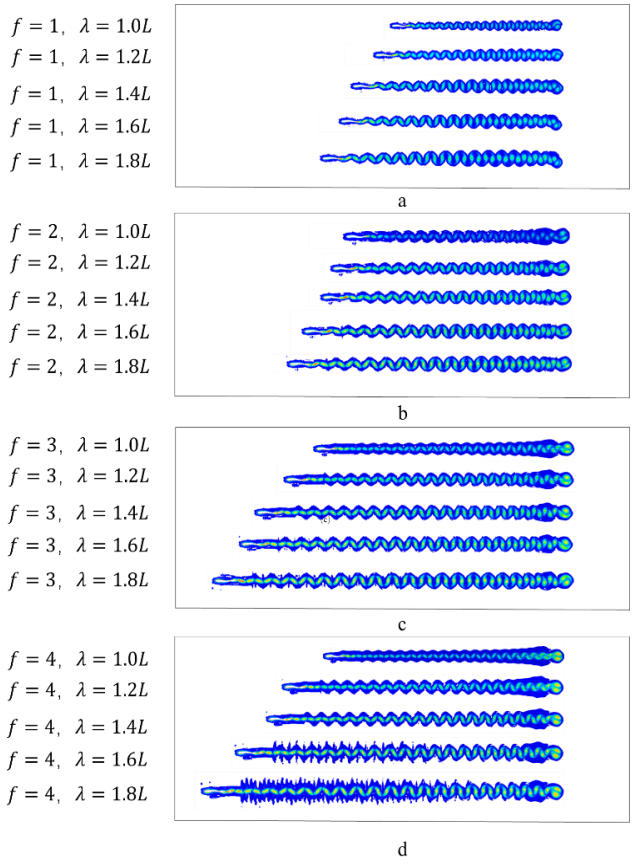

Fig. 4 Vortex trajectory contours: a – frequency = 1 Hz, b – frequency = 2 Hz, c – frequency = 3 Hz, d – frequency = 4 Hz

4.2. Self-propulsion speed performance analysis

The velocity variation trajectory of the flexible hydrofoil reaching steady swimming at different flapping frequencies and oscillation wavelengths is shown in Fig. 5. It can be observed that the motion of the flexible hydrofoil is characterized by variable acceleration. During the transition from rest to steady swimming, the acceleration gradually decreases until it reaches 0. This is because the propulsive force generated by the flexible hydrofoil during swimming remains constant. As the swimming speed increases, the resistance experienced by the flexible hydrofoil also increases. Eventually, when the resistance reaches the same magnitude as the propulsive force generated by the hydrofoil's motion, the net force on the flexible hydrofoil becomes

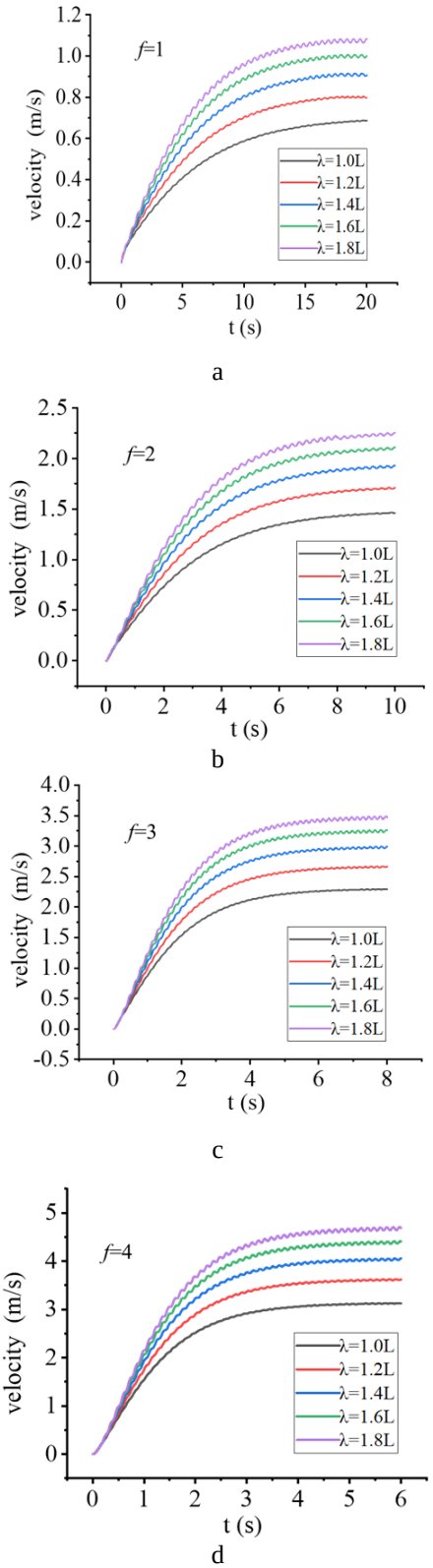

Fig. 5 Trajectory of velocity change as the flexible fins reach uniform swimming speed: a – frequency = 1 Hz, b – frequency = 2 Hz, c – frequency = 3 Hz, d – frequency = 4 Hz

zero, leading to a steady swimming state at a constant velocity. The maximum velocity achieved by the flexible hydrofoil varies with changes in the motion parameters, as shown in Fig. 6.

Furthermore, as the frequency and wavelength of the flexible hydrofoil increase, the size of the trailing vortices, its swimming speed, and the final reached velocity

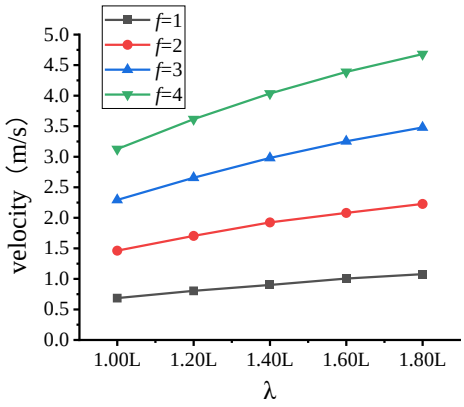

Fig. 6 Trend graph of maximum speed variation

also increase. Under the same frequency, a shorter wavelength leads to more stable diffusion of the trailing vortices, resulting in relatively higher efficiency. When the wavelength is fixed, increasing the frequency leads to larger turbulence generated at the tail of the flexible hydrofoil. This is because a higher frequency corresponds to a higher swimming speed for the flexible hydrofoil. When the flexible hydrofoil flaps with higher stiffness and frequency, it generates more turbulence, which is detrimental to swimming efficiency. In contrast, a more stable trailing vortex leads to higher hydrodynamic efficiency with less turbulence.

4.3. Efficiency analysis of self-propulsion motion

Take the example of a flexible fin swimming at a frequency of 2Hz and a wavelength of 1.0L, the changes of resultant force, velocity, acceleration and displacement of x-axis in the swimming process are shown in the figure below. As we can see, the acceleration is generated by the resultant force in x-axis. The force is the thrust generated by the flexible fins minus the drag force that is experienced. With the increase of the swimming speed of the flexible fin, the fluid resistance increases gradually, and the x-axis resultant force that produces the acceleration decrease gradually, so as the acceleration. At this point, the swimming speed of the flexible fin is gradually constant and reaches the state of uniform swimming speed. This is consistent with the previous analysis.

The trajectory of the acceleration and combined force in x-axis shows sinusoidal fluctuations per unit time. This phenomenon is caused by the reciprocal oscillation of the flexible fins. At a frequency of 2 Hz, the flexible fins oscillate back and forth four times per second, generating four peaks and valleys per second. The peak represents that the tail of the flexible fins reaches the center axis, and the thrust is at its maximum at this time. The trough represents the maximum amplitude reached at the tail of the flexible fin, and the thrust is at its minimum at this time; thrust and acceleration reach peaks and troughs at the same time is consistent with the actual situation.

Secondly, from Fig. 7, when the frequency of the flexible fin fluctuation remains constant, the maximum swimming speed of the flexible fin increases with the growth of wavelength. Similarly, when the wavelength is kept constant, the maximum swimming speed of the flexible fin increases with the rise in frequency.

However, the frequency of fluctuations clearly dominates the change in the maximum swimming speed of

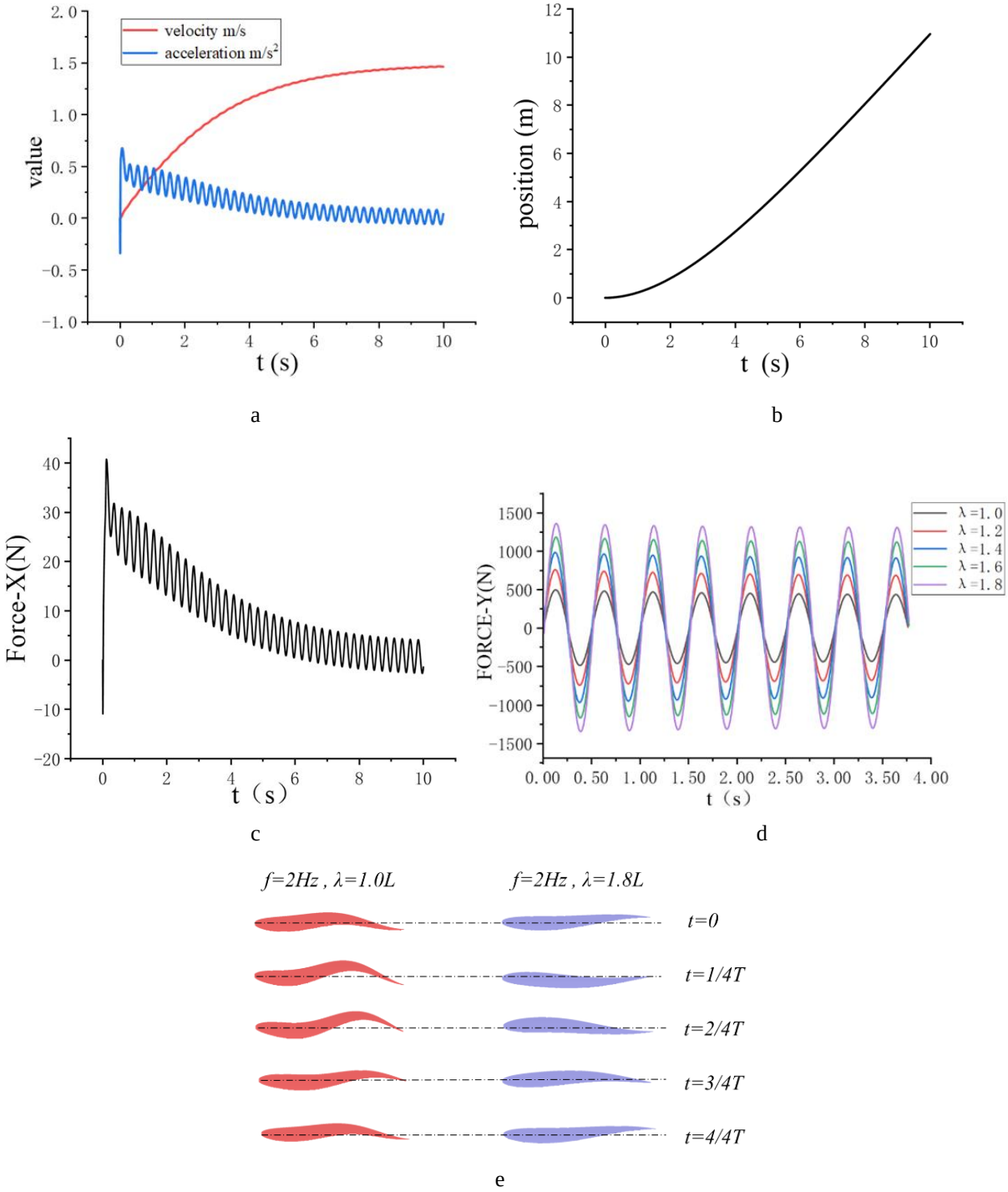

Fig. 7 Flexible fin swim data (f=2, λ=1.0L): a – velocity and acceleration changes, b – location change, c – x-axis combined force, d – y-axis combined force, e – effects of wavelength changes on fins

the flexible fins. There are two reasons for this phenomenon. Firstly, the greater is the frequency, and the faster is its longitudinal fluctuation speed, and the greater is the thrust on the water, and so as the final swimming speed of the flexible fins. Secondly, the longer the wavelength, the more rigid the flexible fins are and the less flexible they are; when the stiffness increases, the deformation of the flexible fins results in greater resistance to reduced longitudinal fluctuations, at which point the conversion efficiency for generating transverse thrust decreases. So the increase in wavelength has a secondary effect on the increase in maximum swimming velocity. Taking 2 Hz frequency as an example, the degree of longitudinal thrust and the deformation of flexible fin for different wavelengths are shown below.

The efficiencies of the flexible fins at different frequencies and different wavelengths when swimming at a constant speed are shown in Table 1, and the trend of their efficiencies is reflected in the surface Fig. 8.

Among them, λ and f are two independent variables, and η is the dependent variable. The intensity of the linear relationship between them needs to be measured by the multiple correlation coefficient. Let the multiple correlation coefficient be R, and calculate the multiple correlation coefficient through Multiple Linear Regression Analysis.

The calculation formula is as follows:

$$\eta = \beta_0 + \beta_1 f + \beta_2 \lambda + \varphi, \tag{15}$$

$$R = \sqrt{\left(1 - \frac{\sum(\eta_i - \hat{\eta}_i)^2}{\sum(\eta_i - \bar{\eta}_i)^2}\right)^2}, \tag{16}$$

where β_0, β_1, and β_2 are the regression coefficients, and φ represents the error term. $\sum(\eta_i - \hat{\eta}_i)^2$ is the residual sum of squares, $\sum(\eta_i - \bar{\eta}_i)^2$ is the total sum of squares, $\hat{\eta}$ is the predicted value from the regression model, and $\bar{\eta}$ is the mean of the dependent variable η.

The computed multiple correlation coefficient $R = 0.9849$ indicates a strong positive linear relationship between λ, f, and η, suggesting that the model has good predictive capability.

As can be observed from the surface plot, the propulsive efficiency decreases with the increases of the wavelength. The main reason is that as the wavelength increases, the flexibility decreases and the efficiency decreases, on the contrary, the greater the fluctuation frequency and flexibility of the flexible fins are, and the better the propulsive efficiency is. This is consistent with the previously mentioned reasons for reduced conversion efficiency.

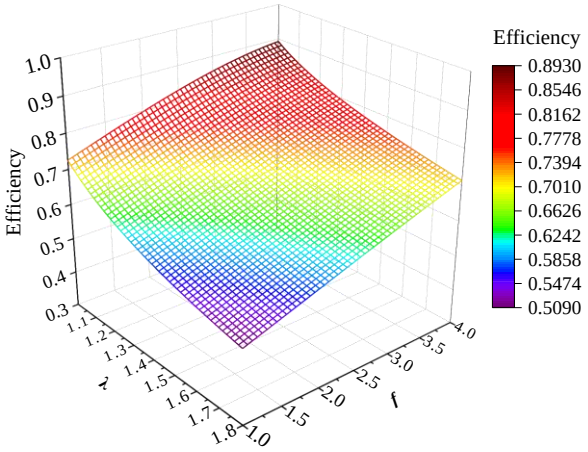

Fig. 8 Uniform swimming efficiency diagram

Table 1

Uniform swimming efficiency

Efficiency	λ =1.0	λ =1.2	λ =1.4	λ =1.6	λ =1.8
f=1	0.727230	0.633499	0.575796	0.540369	0.512078
f=2	0.795669	0.706248	0.651182	0.607000	0.574349
f=3	0.857978	0.767743	0.722768	0.671201	0.653278
f=4	0.893679	0.815068	0.777319	0.740290	0.711257

5. Conclusions

With the development of marine science and technology, the bionic flexible wing propulsion system provides a new design idea for the design and development of underwater vehicle power system with the advantages of high propulsion efficiency and low noise. In this study, numerical simulation methods were used to explore the effect of two dynamic parameters, wavelength and frequency, on the efficiency of the flexible fin thruster. Ray's pectoral fin was simplified into a two-dimensional model, and the three-dimensional overlapping grid technique and the k-ω turbulence model are used. The numerical simulation results were validated against the experimental results of Egan, demonstrating the method's effectiveness.

Through numerical simulations, it was found that as the frequency and wavelength decrease, the swimming speed of the flexible fin slows down while its propulsion efficiency increases. This indicates that flexible fin propulsion exhibits good efficiency at lower speeds, with efficiency reaching up to 89% in this study. When the flapping frequency of the flexible fin increases, muscle contraction leads to increased stiffness, equivalent to an increase in wavelength. When the flexible fin flaps with high frequency and large wavelength parameters, it behaves similarly to the burst-sprint swimming state, where increased muscle contraction stiffness leads to reduced swimming efficiency but a substantial increase in swimming speed.

Based on the simplified model used in this study's numerical simulations, the effect of dynamic parameters on the self-propulsion performance of flexible fins was to some extent reflected. However, compared to the actual propulsion of rays, the simplified model remains ideal and leaves ample room for improvement. To achieve underwater vehicles with biomimetic efficiency similar to aquatic organisms, further exploration is necessary.

References

1. **Hanshin, S.; Paik, B. G.** 2019. Correlation study between propeller noise and cavitation erosion with inclined propeller model test, The Journal of the Acoustical Society of Korea, 38(3):328-333. https://doi.org/10.7776/ASK.2019.38.3.328.
2. **Seol, H.** 2018. Experimental Study on the Cavitation Noise Characteristics of Model Propeller in Uniform Inflow, Transactions of the Korean Society for Noise and Vibration Engineering 28(6):728-734. https://doi.org/10.5050/KSNVE.2018.28.6.728.
3. **Cervello, G.; Olivier, F.; Chauvaud, L.; Winkler, G.; Mathias, D.; Juanes, F.; Tremblay, R.** 2023. Impact of anthropogenic sounds (pile driving, drilling and vessels) on the development of model species involved in marine biofouling, Frontiers in Marine Science 10: 1111505. https://doi.org/10.3389/fmars.2023.1111505.
4. **Escajeda, E. D.; Stafford, K. M.; Woodgate, R. A.; Laidre, K. L.** 2023. Quantifying the effect of ship noise on the acoustic environment of the Bering Strait, Marine Pollution Bulletin 187: 114557. https://doi.org/10.1016/j.marpolbul.2022.114557.
5. **Rising, K.; Hardege, J.; Tregenza, T.; Stevens, M.** 2022. Anthropogenic noise may impair the mating behaviour of the Shore Crab Carcinus Maenas, Plos One: e0276889. https://doi.org/10.1371/journal.pone.0276889.

6. **Williams, T. M.; Blackwell, S. B.; Tervo, O.; Garde, E.; Sinding, M. H.; Richter, B.; Heide-Jorgensen, M. P.** 2022. Physiological responses of narwhals to anthropogenic noise: A case study with seismic airguns and vessel traffic in the Arctic, Functional Ecology 36(9): 2251-2266. https://doi.org/10.1111/1365-2435.14119.
7. **Zhang, D.; Pan, G.; Cao, Y.; Huang, Q.; Cao, Y.** 2022. A Novel Integrated Gliding and Flapping Propulsion Biomimetic Manta-Ray Robot, Journal of Marine Science and Engineering 10(7): 924. https://doi.org/10.3390/jmse10070924.
8. **Yu, J.; Wang, M.; Dong, H.; Zhang, Y.; Wu, Z.** 2018. Motion Control and Motion Coordination of Bionic Robotic Fish: A Review, Journal of Bionic Engineering 15(4): 579-598. https://doi.org/10.1007/s42235-018-0048-2.
9. **Yin, X.; Jia, L.; Wang, C.; Xie, G.** 2016. Modelling of thrust generated by oscillation caudal fin of underwater bionic robot, Applied Mathematics and Mechanics-English Edition 37(5): 601-610. https://doi.org/10.1007/s10483-016-2074-8.
10. **Xia, X.; Hu, N.; Liu, J.; Chen, G.; Yang, Q.; Chen, Y.** 2021. Development and Innovative Design Research of Underwater Bionic Fish Products under Hybrid Propulsion Technology, Wireless Communications and Mobile Computing 2021: 5146992. https://doi.org/10.1155/2021/5146992.
11. **Vogel, S.** 2008. Modes and scaling in aquatic locomotion, Integrative and Comparative Biology 48(6): 702-712. https://doi.org/10.1093/icb/icn014.
12. **Saadat, M.; Fish, F. E.; Domel, A.G.; Di Santo, V.; Lauder. G.V.; Haj-Hariri, H.** 2017. On the rules for aquatic locomotion, Physical Review Fluids 2(8): 083102. https://doi.org/10.1103/PhysRevFluids.2.083102.
13. **Han, P.; Lauder, G. V.; Dong, H.** 2020. Hydrodynamics of median-fin interactions in fish-like locomotion: Effects of fin shape and movement, Physics of Fluids 32(1): 011902. https://doi.org/10.1063/1.5129274.
14. **Gadig, O. B. F.; Neto, D. G.** 2014. Notes on the feeding behaviour and swimming pattern of Manta alfredi (Chondrichthyes, Mobulidae) in the Red Sea, Acta Ethologica 17(2): 119-122. https://doi.org/10.1007/s10211-013-0165-1.
15. **Menzer, A.; Gong, Y.; Fish, F. E.; Dong, H.** 2022. Bio-Inspired Propulsion: Towards Understanding the Role of Pectoral Fin Kinematics in Manta-like Swimming, Biomimetics 7(2): 45. https://doi.org/10.3390/biomimetics7020045.
16. **Gao, P. C.; Huang, Q. G.; Pan, G.; Song, D.; Cao, Y.** 2023. Research on swimming performance of fish in different species. Physics of Fluids 35(6): 1909. https://doi.org/10.1063/5.0154914.
17. **Dewar, H.; Mous, P.; Domeier, M.; Muljadi, A.; Pet, J.; Whitty, J.** 2008. Movements and site fidelity of the giant manta ray, Manta birostris, in the Komodo Marine Park, Indonesia, Marine Biology 155(2): 121-133. https://doi.org/10.1007/s00227-008-0988-x.
18. **Rosenberger, L. J.** 2001. Pectoral Fin Locomotion in Batoid Fishes: Undulation Versus Oscillation, The Journal of Experimental Biology 204(2): 379-394. https://doi.org/10.1242/jeb.204.2.379.
19. **Zhang, D.; Huang, Q. G.; Pan, G.; Yang, L. M.; Huang, W. X.** 2022. Vortex dynamics and hydrodynamic performance enhancement mechanism in batoid fish oscillatory swimming, Journal of Fluid Mechanics 930: A28. https://doi.org/10.1017/jfm.2021.917.
20. **Russo, R. S.; Blemker, S. S.; Fish, F. E.; Bart-Smith, H.** 2015. Biomechanical model of batoid (skates and rays) pectoral fins predicts the influence of skeletal structure on fin kinematics: implications for bio-inspired design, Bioinspiration and Biomimetics 10(4): 046002. https://doi.org/10.1088/1748-3190/10/4/046002.
21. **Cao, Y.; Bao, T.; Cao, Y.; Wang, P.; Yang, O.; Lu, Y.; Cao, Y.** 2022. Effects of Bionic Bone Flexibility on the Hydrodynamics of Pectoral Fins, Journal of Marine Science and Engineering 10(7): 981. https://doi.org/10.3390/jmse10070981.
22. **Meng, Y.; Wu, Z.; Dong, H.; Wang, J.; Yu, J.** 2022. Toward a Novel Robotic Manta With Unique Pectoral Fins, IEEE Transactions on Systems, Man and Cybernetics: Systems 52(3): 1663-1673. https://doi.org/10.1109/TSMC.2020.3034503.
23. **Cao, Y. H.; Ma, S. M.; Cao, Y. Z.; Pan, G.; Huang, Q. G.; Cao, Y.** 2022. Similarity Evaluation Rule and Motion Posture Optimization for a Manta Ray Robot, Journal of Marine Science and Engineering 10(7): 908. https://doi.org/10.3390/jmse10070908.
24. **Liu, Q. M.; Chen, H.; Wang, Z. H.; He, Q.; Chen, L. K.; Li, W. K.; Li, R. P.; Cui, W.C.** 2022. A Manta Ray Robot with Soft Material Based Flapping Wing, Journal of Marine Science and Engineering 10(7): 962. https://doi.org/10.3390/jmse10070962.
25. **Thekkethil, N.; Sharma, A.; Agrawal, A.** 2020. Three-dimensional biological hydrodynamics study on various types of batoid fishlike locomotion, Physical Review Fluids 5(2): 023101. https://doi.org/10.1103/PhysRevFluids.5.023101.
26. **Fish, F. E.; Kolpas, A.; Crossett, A.; Dudas, M. A.; Moored, K. W.; Bart-Smith, H.** 2018. Kinematics of swimming of the manta ray: three-dimensional analysis of open-water maneuverability, Journal of Experimental Biology 221(6): jeb166041. https://doi.org/10.1242/jeb.166041.
27. **Moored, K. W.; Fish, F. E.; Kemp, T. H.; Bart-Smith, H.** 2011. Batoid Fishes: Inspiration for the Next Generation of Underwater Robots, Marine Technology Society Journal 45(4): 99-109. https://doi.org/10.4031/MTSJ.45.4.10.
28. **Fish, F. E; Dong, H.; Zhu, J. J.; Bart-Smith, H.** 2017. Kinematics and Hydrodynamics of Mobuliform Swimming: Oscillatory Winged Propulsion by Large Pelagic Batoids, Marine Technology Society Journal 51(5): 35-47. https://doi.org/10.4031/MTSJ.51.5.5.
29. **Fish, F. E.; Schreiber, C.; Moored, K.; Liu, G.; Dong, H.; Bart-Smith, H.** 2016. Hydrodynamic Performance of Aquatic Flapping: Efficiency of Underwater Flight in the Manta, Aerospace 3(3): 20. https://doi.org/10.3390/aerospace3030020.
30. **Hu, P.; Li, Y.; Cai, C. S.; Liao, H.; Xu, G. J.** 2013. Numerical simulation of the neutral equilibrium atmospheric boundary layer using the SST k-ω turbulence model, Wind and Structures, 17(1): 87-105.

http://dx.doi.org/10.12989/was.2013.17.1.087.
31. **Doi, K.; Takagi, T.; Mitsunaga, Y.; Torisawa, S.** 2021. Hydrodynamical effect of parallelly swimming fish using computational fluid dynamics method. PLoS One 16(5): e0250837. https://doi.org/10.1371/journal.pone.0250837.
32. **Egan, B. C.; Brownell, C. J.; Murray, M. M.** 2016. Experimental assessment of performance characteristics for pitching flexible propulsors, Journal of Fluids and Structures 67: 22-33. https://doi.org/10.1016/j.jfluidstructs.2016.09.003.

H. Ding, Q. Gao, H. Shi, H. Shen, R. Chen

EFFECT OF MANTA RAY'S FLEXIBLE HYDROFOIL KINEMATIC PARAMETERS ON AUTONOMOUS PROPULSION EFFICIENCY

S u m m a r y

In this study, an overlapping grid was used to create a simplified model based on the pectoral fins of a manta ray. The oscillatory traveling wave equation is programmed and loaded on the pectoral fin model to characterize the motion state of the manta ray cross-section. It explored how wavelength and frequency affect the efficiency of flexible hydrofoil swimming. Results showed that flexible hydrofoils create reverse Kármán vortex streets during autonomous swimming. The size of these vortices, along with frequency and wavelength, impacts propulsive efficiency. When frequency is fixed, increasing wavelength increases turbulence, reducing efficiency but slightly boosting speed. Conversely, fixing wavelength and increasing frequency improves stability, enhancing efficiency and speed. This research offers new insights for designing biomimetic underwater propulsion systems in marine engineering.

Keywords: manta ray, flexible hydrofoil, CFD, self-propelled swimming, propulsion efficiency.

Received June 22, 2024
Accepted December 16, 2024